Femtosecond-Terawatt Hard X-Ray Pulse Generation with Chirped Pulse Amplification on a Free Electron Laser

Haoyuan Li,* James MacArthur, Sean Littleton,† Mike Dunne, Zhirong Huang,† and Diling Zhu‡
Linac Coherent Light Source, SLAC National Accelerator Laboratory, Menlo Park, California 94025, USA

(Received 11 March 2022; accepted 21 October 2022; published 18 November 2022)

Advances of high intensity lasers have opened up the field of strong field physics and led to a broad range of technological applications. Recent x-ray laser sources and optics development makes it possible to obtain extremely high intensity and brightness at x-ray wavelengths. In this Letter, we present a system design that implements chirped pulse amplification for hard x-ray free electron lasers. Numerical modeling with realistic experimental parameters shows that near-transform-limit single-femtosecond hard x-ray laser pulses with peak power exceeding 1 TW and brightness exceeding 4×10^{35} s^{-1} mm^{-2} $mrad^{-2}0.1\%$ $bandwdith^{-1}$ can be consistently generated. Realization of such beam qualities is essential for establishing systematic and quantitative understanding of strong field x-ray physics and nonlinear x-ray optics phenomena.

DOI: 10.1103/PhysRevLett.129.213901

High-intensity high-brightness x-ray pulses from free electron lasers (FEL) have opened up many new routes of research for strong field physics [1,2], nonlinear x-ray optics, and many potential applications [3–12]. While the past decade has witnessed many *first demonstrations*, one major obstacle towards a quantitative, systematic, and application-oriented understanding of the subject came from the stochastic temporal and spectral structure of the pulses [13]. Production of terawatt-femtosecond (TW-fs) hard x-ray pulses with full spatial and temporal coherence is therefore highly desired. This calls for allround improvement of the x-ray beam quality, including peak intensity, peak brightness, and a well-defined spatial temporal profile, which are mandatory for quantitative analysis and prediction of the nonlinear observables.

Currently, the peak power of a state-of-the-art FEL can reach 100 GW scale [14] through self-amplified spontaneous emission (SASE). To push the peak power into TW scale, several enhanced-SASE schemes [15–17] have projected terawatt-attosecond (TW-as) output by using extremely high peak current. A super-radiance based approach [18] was shown to be capable of delivering TW hard x-ray pulses with a sequence of short electron bunches and electron and optical delay devices. These approaches still inherited the rugged temporal characteristics of SASE, while also requiring electron beam parameters beyond the current state-of-art. Self-seeding techniques were adopted to improve the temporal coherence up on SASE [19–22] with impressive peak brightness improvement. However, the narrow bandwidth puts a limit on attainable pulse duration and peak power. In this Letter, we present the design and performance evaluation of a hard x-ray chirped pulse amplification (CPA) setup that can potentially deliver single-femtosecond x-ray pulses with a clean temporal profile and provide high peak power (>1 TW) and high peak spectral brightness at the same time.

At optical wavelength, CPA has revolutionized high intensity pulse generation and its applications [23,24]. The concept has been extended to the extreme-ultraviolet wavelengths [25]. At Å wavelength, an earlier proposal [26] used chirped electron bunches to generate chirped x-ray pulses before the compression by an optical compressor. Detailed analysis [27] showed that, however, electron bunch manipulation alone cannot produce temporal chirp of sufficient magnitude and quality, leading to limited compression ratio and low photon throughput at the compressor. We overcome this limitation by a complete CPA scheme consisting of both optical stretcher and compressor. This gave us precise control of the temporal chirp, realizing two seemingly competing quantities in an FEL: a relatively wide bandwidth required by the short final pulse duration and the long and uniform pulse temporal profile during amplification to extract as much energy from the electron bunch as possible, simultaneously. The system design is illustrated schematically in Fig. 1(a), where bold green labels are used to indicate the names of different parts.

In this hypothetical setup, the undulator segments are divided into two groups: the seed section and the amplifier section. We use two electron bunches with nanosecond time separation [28] to serve as the seed and amplification gain media, respectively. The seed electron bunch is short with high peak current. The amplifier electron bunch is longer and contains higher total charge. In the seed section, the first electron bunch produces a short and intense hard x-ray pulse while the trailing amplifier electron bunch travels along a lasing-suppressed orbit. Exiting the seed section, the seed pulse propagates through a crystal-optic

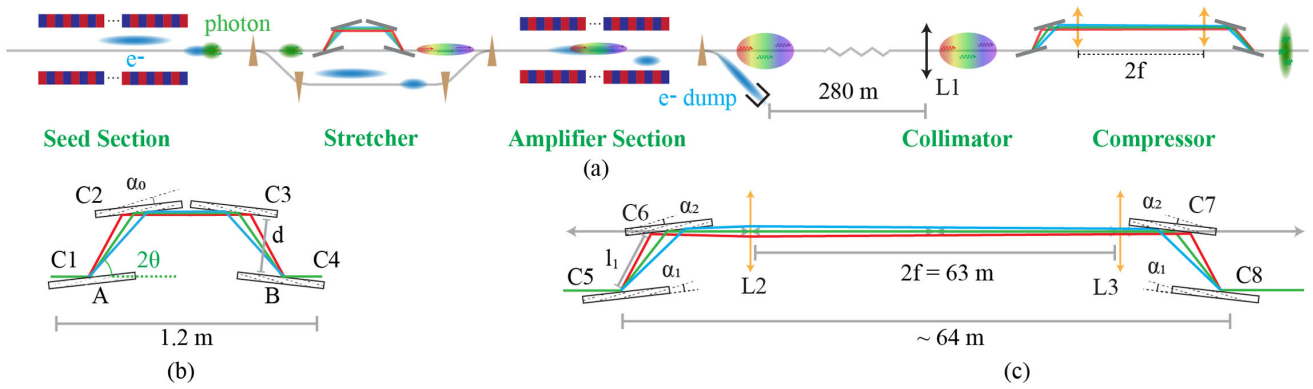

FIG. 1. (a) Layout of the setup. The symbols $C1$ to $C8$ represent Bragg crystals to guide the trajectory of the x-ray pulse. (b) Schematics of the stretcher. (c) Schematics of the compressor.

stretcher, and obtains a strong temporal chirp while expanding significantly in pulse duration, matching that of the amplifier electron bunch. The electron bunches are diverted away from the stretcher optics after the seed section with a magnetic chicane. The crystal stretcher introduces a time delay to the seed x-ray pulse by the exact amount as the time spacing between the seed and amplifier electron bunches. This enables interaction between the stretched seed x-ray pulse and the second electron bunch to achieve amplification in the amplifier section of the undulator, where the seed electron bunch is directed to a lasing-suppressed orbit. Exiting the amplifier section, both electron bunches are diverted to the electron beam dump. The amplified, saturated, and chirped hard x-ray pulse propagates downstream to a crystal optic compressor, where we remove the temporal chirp to reach a much shorter pulse duration and higher peak power.

To understand the potential performance envelope of this CPA scheme, detailed numerical modeling is required. The chosen electron beam parameters for the seed and amplifier bunches are summarized in Table I, all of which have been demonstrated at many current FEL facilities, such as LCLS. A total of 32 undulator segments as currently installed at the LCLS-II hard x-ray beamline were assumed. We used *Genesis* [29] to predict the electron lasing dynamics in both undulator sections. The crystal optics is simulated with a homebuilt beam propagation program, the source code of which can be found in Ref. [30]. The two-beam dynamical diffraction theory [31] is used to describe the reflection, angular dispersion, and absorption of crystal optics and transmission optics. The operation photon energy is chosen to be 9.5 keV.

TABLE I. Beam parameters used in *Genesis* simulations.

	1st electron bunch	2nd electron bunch
Bunch charge	7.5 pC	200 pC
Bunch length	0.375 μm	20 μm
Emittance	0.4 μm	0.4 μm
Energy spread	3.49 GeV	2.06 MeV
Current profile	Flat-top	Flat-top
Peak current	6 kA	3 kA
Taper	Flat	Genesis-informed
K	2.4	2.4
Electron energy	10 GeV	10 GeV

The schematics of the stretcher is shown in Fig. 1(b). This is a direct analog of the corresponding device at optical wavelengths [32]. The stretcher consists of 4 crystals, $C1$ to $C4$, arranged in a mirror symmetric layout, with asymmetric Bragg reflections. Because of the angular dispersion of asymmetric Bragg reflections, x-ray photons with different energies follow different trajectories inside the stretcher, indicated by different colors in Fig. 1(b), which leads to a light path length difference. Define θ to be the Bragg angle, α_0 the asymmetry angle of the Bragg reflection, d the gap size of the crystal pairs $C1/C2$ and $C3/C4$, and E_0 the reference photon energy. With ray-tracing analysis, the energy dependence of the path length inside the stretcher can be shown to be

$$\delta(L) \approx -8d\frac{\sin^2\alpha_0\sin^2\theta}{\sin^3(\alpha_0+\theta)}\times\frac{\delta E}{E_0}, \tag{1}$$

where δE is the energy difference with respect to E_0. Note that higher energy x rays always have a shorter path length. This thus always creates a negative temporal chirp regardless of the sign of α_0.

A large bandwidth and high reflectivity are desired, in order to obtain higher seed pulse energy, and reduce potential compressed pulse duration. We choose Si (111) reflections for $C1$ to $C4$, with an asymmetry angle of 10° to produce the required angular dispersion and increase the bandwidth. At $E_0 = 9.5$ keV, the Bragg angle is $\theta = 12.02°$. As shown in Fig. 1(b), the beam adopts grazing incidence geometry on $C_1/C3$, and grazing exit geometry on $C2/C4$. The gap size d must be chosen to match the

stretcher delay to the time separation between the two electron bunches, which can only be multiples of 0.35 ns, determined by of the radio-frequency (rf) of the accelerator [33]. Following geometric optics, the relation between stretcher delay T_{delay} and gap size d can be shown to be

$$T_{\mathrm{delay}} = \frac{2d}{c}\frac{(1-\cos 2\theta)}{\sin(\theta-\alpha_0)}, \tag{2}$$

where c is the speed of light in vacuum. Therefore, the available gap sizes are $d \in \{2.1\ \mathrm{mm}, 4.3\ \mathrm{mm}, \cdots\}$. The $d = 2.1$ mm is chosen in order to match the stretched seed pulse duration to the amplifier electron bunch length, which is limited to a maximum of ~60 fs if we want to maintain the optimal peak current of 3 kA. At $d = 2.1$ mm, simulation of 60 seed SASE pulses with a FWHM pulse duration of 0.6 ± 0.6 fs at 9.5 keV yielded FWHM pulse duration after the stretcher at 43.8 ± 11.3 fs.

Using the stretcher parameters specified above, we next optimize the distribution of undulator segments between the seed section and amplifier section. In total, 6 configurations are compared, from 7 to 17 undulator segments assigned to the seed section with increments of 2. The rest of the undulator segments are assigned to the amplifier section. For each configuration, 10 simulations of the FEL pulse energy growth trajectory are summarized in Fig. 2(a), with different colors representing different undulator allocation schemes. One can see that when the number of seed undulators reaches 13, the pulse energy of the seed pulse after the stretcher saturates. Allocating additional seed segments would not increase the seed power but rather would impose higher thermal load to the first crystal of the stretcher. The on-axis phase of each pulse as shown in Fig. 2(b), one sees the prominent parabolic phase curves across all settings, indicating that the electron dynamics in the amplifier section preserves the temporal chirp very well except for the seven-seed-segment case, where the seed power is too low. The compressor has a similar bandwidth as the stretcher. Therefore the weak parasitic SASE radiation will be filtered out by the compressor. Reconciling the desire for a strong seed pulse, low crystal thermal load, and the preservation for temporal chirp, we choose the configuration with 13 seed undulators. We then apply a *Genesis*-informed taper optimization for this configuration. The resulting average x-ray pulse energy is 2.9 ± 0.8 mJ at the exit of amplifier section for the simulation presented below.

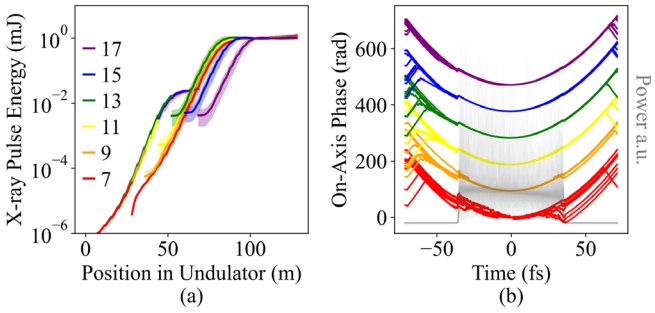

FIG. 2. (a) The evolution of the x-ray pulse energy along the undulator sections for different configurations. The number in the legend is the number of undulator segments assigned to the seed section. The solid lines represent the averaged pulse energy over 10 simulated pulses in each configuration. The shaded area indicates the standard deviation of the pulse energy of the 10 pulses. (b) The on-axis phase of x-ray pulses at the exit of the amplifier section. Each solid line represents the phase of a single simulated pulse. The color scheme and its meaning is the same as that of subplot (a). The gray shadow indicates the power profile of all 70 pulses.

The four-bounce structure used in the stretcher cannot generate positive temporal chirps. To generate a positive chirp, we adopt the Martinez stretcher [34] scheme to the hard x-ray wavelengths. The layout of the compressor is shown in Fig. 1(c). Crystals $C5$ to $C8$ are arranged mirror symmetrically with respect to two focusing lenses, $L2$ and $L3$, in between. To match the bandwidth, $C5$ to $C8$ also use silicon (111) asymmetric Bragg reflections. The asymmetry angle of $C5$ and $C8$ is α_1. The asymmetry angle of $C6$ and $C7$ is α_2 and $\alpha_1 \neq \alpha_2$. Both focusing lenses have the same focal length, f, and form a telescope with a magnification factor of 1. Because $\alpha_1 \neq \alpha_2$, the crystal pair $C5$-$C6$ leads to a net angular dispersion, which is compensated by $C7$-$C8$. Between $C6$ and $C7$, the telescope converts this angular dispersion into spectral-temporal chirp. Assume that the path length between the beam footprints within crystal pairs $C5$-$C6$ and $C7$-$C8$ is l_1, the distance between crystal $C6$ or $C7$ and their adjacent focusing lens is negligible compared with the focal length f. Then, the energy dependence of the path length in the compressor can be attributed to primarily two components:

$$\delta(L) \approx -8l_1 \frac{\sin^2\alpha_1 \sin^2\theta}{\sin^2(\alpha_1+\theta)} \times \frac{\delta E}{E_0} + 8f \frac{\sin^2(\alpha_1-\alpha_2)\sin^4\theta}{\sin^2(\alpha_1+\theta)\sin^2(\alpha_2-\theta)} \times \frac{\delta E}{E_0}. \tag{3}$$

The first term, resembling the energy dependence of the stretcher, shows that the propagation within $C5$-$C6$ and $C7$-$C8$ introduces negative temporal chirp. The second term represents a positive temporal chirp proportional to the focal length f. By choosing a proper set of f, α_1, and α_2, a net positive temporal chirp can be generated. The derivation of Eq. (3) is summarized in the Supplemental Material [35].

The compressor parameters are determined by the balance between the bandwidth and reflectivity of Bragg reflections with different asymmetry angles. Bandwidth increase from the amplification process also needs to be considered. To maximize the final peak power, we surveyed the asymmetry angles α_2 of $C6$ and $C7$ from 10° to 10.7° with a step size of 0.1° in the numerical simulation. In each step, the focal

length f is optimized with increments of 0.1 m to obtain the highest peak power. In this process, we choose $\alpha_1 = \alpha_2 + 0.2°$ to generate a nonzero angular dispersion with $C5$-$C6$ for the telescope to generate the positive temporal chirp. This angle difference is chosen such that f is neither too short such that the lens loss becomes significant, nor too long such that the whole setup cannot reside within the existing LCLS x-ray transport tunnel. In the simulation, the transmission function of the two lens are calculated assuming a parabola shape function with the actual complex refractive index of the beryllium. This optimization step yielded $\alpha_1 = 10.7°$, $\alpha_2 = 10.5°$, and $f = 31.5$ m.

The angular dispersion introduced by $C5$-$C6$ varies slightly for different incident angles. This will reduce the compression ratio. To mitigate this effect, the amplified pulse is collimated before entering the compressor. Specifically, after exiting the amplifier section, the amplified pulse propagates 280 m in free space, and passes through a focusing lens, $L1$, with a focal length of 315 m. After the collimation, at the position of $C5$ of the compressor, the averaged FWHM angular divergence of the pulse is 0.1 ± 0.04 μrad, and the average FWHM pulse size is 444.7 ± 52.4 μm, a beam condition where existing silicon monochrometers have operated under similar beam energy (3–4 mJ) without observable performance degradation. Figure 3 shows the temporal and spectral evolution of one typical simulation using this configuration. The seed pulse had a FWHM pulse duration of 0.7 fs. The stretcher extended the pulse to 47.5 fs in FWHM with an energy efficiency of 59% within the bandwidth of 9.498-to-9.502 keV, and 35% over the whole spectrum. After the amplification, the FWHM pulse duration increased to 62.3 fs. Finally, after the compression, the FWHM pulse duration was reduced to 1.3 fs, with an energy efficiency of 52% through the compressor. The peak power reached 1.2 TW.

The statistical distributions of 10 independent simulations are shown in Fig. 4. The incident FWHM pulse duration was 0.6 ± 0.2 fs with a median value of 0.6 fs. The stretched pulse duration was 46.9 ± 9.2 fs with a median value of 47.8 fs, which resulted in a stretching ratio of 79.1. The total energy efficiency of the stretcher was $24\% \pm 13\%$ with a median value of 24% over the whole spectrum. At the exit of the amplifier section, the averaged pulse duration was 56.8 ± 5.7 fs with a median value of 59.7 fs. After the compression, the pulse duration was reduced to 1.4 ± 0.2 fs with a median value of 1.3 fs, which corresponded to a compression ratio of 40.6. The total energy efficiency of the compressor was $51\% \pm 2\%$ with a median value of 52%. Out of the 10 pulses, 7 of them had peak power greater than 1 TW, and peak brightness exceeding 4×10^{35} s^{-1} mm^{-2} $mrad^{-2}$ 0.1% $bandwidth^{-1}$. Besides, as shown in Fig. 4(d), all pulses except the lowest two pulses feature a single main peak without any prepulses, which can be easily removed from the dataset by a simple pulse energy filter. This is of great importance for strong field physics studies, since signals from weak prepulses can pose significant challenges in accurate data interpretation.

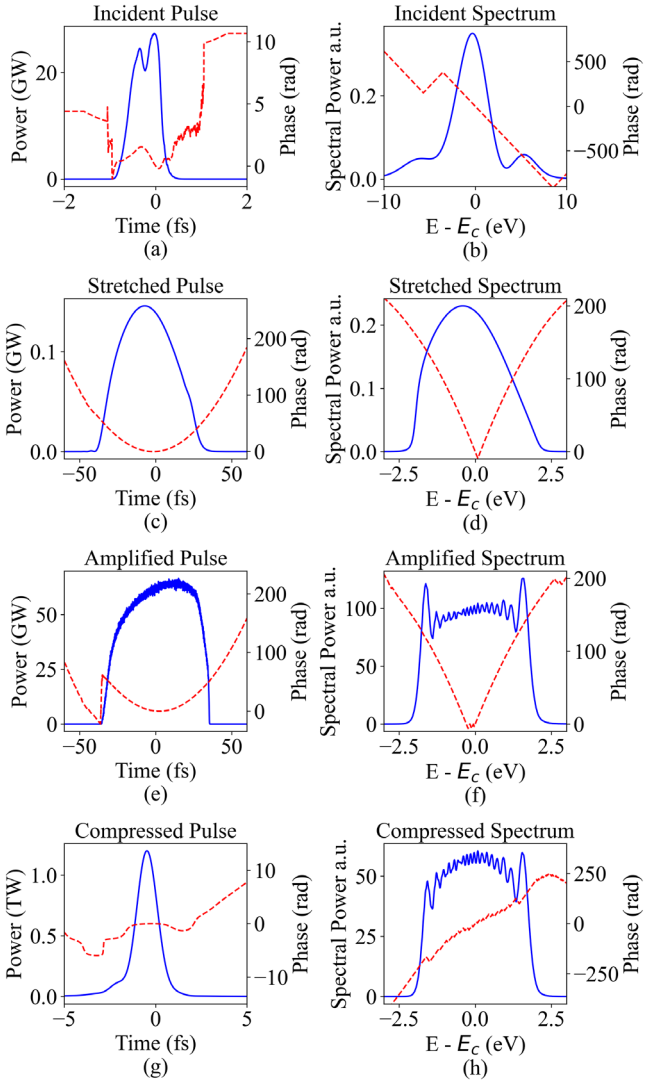

FIG. 3. The subplots (a),(c),(e) and (g) show the power profile (blue solid line) and the phase (red dashed line) on axis. The (b), (d),(f) and (h) show the spectrum profile (blue solid line) and the phase (red dashed line) on axis.

To summarize, detailed feasibility study showed that by extending chirped pulse amplification to hard x-ray wavelengths using crystal optics based pulse stretcher and compressor, near-transform-limited TW-fs hard x-ray pulses can be consistently generated, using electron beam parameters well within the reach of existing free electron laser facilities. The resulting high peak power and brightness will greatly enhance the performance of many current x-ray FEL experiments such as nonlinear x-ray spectroscopy based on various emerging nonlinear x-ray optics phenomena [4,5,36–38]. This opens up new opportunities to track, understand, and control electronic processes in

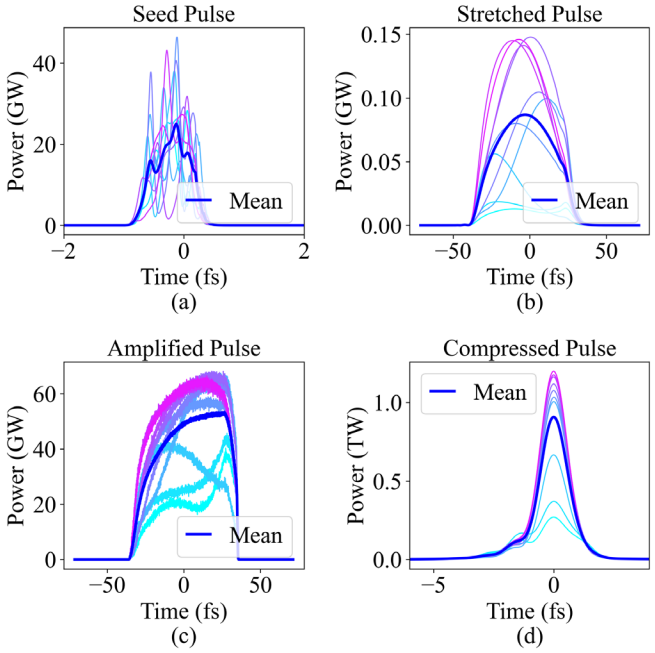

FIG. 4. Power profiles of 10 simulated pulses at 4 different stages indicated by their titles. Thin lines with different colors (except blue) represent each single pulse. The thick blue line represents the averaged beam profile of the 10 pulses.

molecules [39–43]. The relatively narrow bandwidth of x-ray pulses and the resulting clean temporal structure of the x-ray pulses will greatly facilitate the quantitative data interpretation of higher order x-ray nonlinear phenomena, a prerequisite for developing future applications.

The proposed optical layout is flexible in optics parameters, can be tailored for different photon energies, and optimized for different existing x-ray FEL facility infrastructures. Further advancement in electron beam parameters, utilization of higher compression ratio, availability of additional undulator length, will enable another leap in peak power and brightness. The proposed approach is also another example of a concerted-action between electron beam optics and x-ray optics for advancing x-ray FEL performance. One can expect that, in the near future, coherent interplay between crystal optics and free-electron-laser can further enhance our capability to control the lasing dynamics of high brightness electron beams.

The authors thank D. Reis and G. Marcus for helpful discussions. This work is supported by the U.S. Department of Energy, Office of Science, Office of Basic Energy Sciences under Contract No. DE-AC02-76SF00515.

*Also at Physics Department, Stanford University, Stanford, California 94305, USA.
†Also at Applied Physics Department, Stanford University, Stanford, California 94305, USA.
‡dlzhu@slac.stanford.edu

[1] M. Fuchs, M. Trigo, J. Chen, S. Ghimire, S. Shwartz, M. Kozina, M. Jiang, T. Henighan, C. Bray, G. Ndabashimiye *et al.*, Anomalous nonlinear x-ray compton scattering, Nat. Phys. **11**, 964 (2015).
[2] D. Krebs, D. A. Reis, and R. Santra, Time-dependent QED approach to x-ray nonlinear Compton scattering, Phys. Rev. A **99**, 022120 (2019).
[3] S. Shwartz, M. Fuchs, J. B. Hastings, Y. Inubushi, T. Ishikawa, T. Katayama, D. A. Reis, T. Sato, K. Tono, M. Yabashi, S. Yudovich, and S. E. Harris, X-Ray Second Harmonic Generation, Phys. Rev. Lett. **112**, 163901 (2014).
[4] S. Yamamoto *et al.*, Element Selectivity in Second-Harmonic Generation of $GaFeO_3$ by a Soft-X-Ray Free-Electron Laser, Phys. Rev. Lett. **120**, 223902 (2018).
[5] R. K. Lam *et al.*, Soft X-Ray Second Harmonic Generation as an Interfacial Probe, Phys. Rev. Lett. **120**, 023901 (2018).
[6] A. Schori, C. Bömer, D. Borodin, S. P. Collins, B. Detlefs, M. Moretti Sala, S. Yudovich, and S. Shwartz, Parametric Down-Conversion of X Rays into the Optical Regime, Phys. Rev. Lett. **119**, 253902 (2017).
[7] S. Sofer, O. Sefi, E. Strizhevsky, H. Aknin, S. Collins, G. Nisbet, B. Detlefs, C. J. Sahle, and S. Shwartz, Observation of strong nonlinear interactions in parametric down-conversion of x-rays into ultraviolet radiation, Nat. Commun. **10**, 5673 (2019).
[8] D. Krebs and N. Rohringer, Theory of parametric x-ray optical wavemixing processes, arXiv:2104.05838.
[9] T. Kroll *et al.*, Stimulated X-Ray Emission Spectroscopy in Transition Metal Complexes, Phys. Rev. Lett. **120**, 133203 (2018).
[10] T. Glover, D. Fritz, M. Cammarata, T. Allison, S. Coh, J. Feldkamp, H. Lemke, D. Zhu, Y. Feng, R. Coffee *et al.*, X-ray and optical wave mixing, Nature (London) **488**, 603 (2012).
[11] G. Marcus, G. Penn, and A. A. Zholents, Free-Electron Laser Design for Four-Wave Mixing Experiments with Soft-X-Ray Pulses, Phys. Rev. Lett. **113**, 024801 (2014).
[12] S. Mukamel, Multiple core-hole coherence in x-ray four-wave-mixing spectroscopies, Phys. Rev. B **72**, 235110 (2005).
[13] E. Saldin, E. Schneidmiller, and M. Yurkov, Statistical properties of the radiation from SASE FEL operating in the linear regime, Nucl. Instrum. Methods Phys. Res., Sect. A **407**, 291 (1998).
[14] M. W. Guetg, A. A. Lutman, Y. Ding, T. J. Maxwell, F.-J. Decker, U. Bergmann, and Z. Huang, Generation of High-Power High-Intensity Short X-Ray Free-Electron-Laser Pulses, Phys. Rev. Lett. **120**, 014801 (2018).
[15] A. A. Zholents, Method of an enhanced self-amplified spontaneous emission for x-ray free electron lasers, Phys. Rev. ST Accel. Beams **8**, 040701 (2005).
[16] S. Kumar, Y. W. Parc, A. S. Landsman, and D. E. Kim, Temporally-coherent terawatt attosecond xfel synchronized with a few cycle laser, Sci. Rep. **6**, 37700 (2016).
[17] C. H. Shim, Y. W. Parc, S. Kumar, I. S. Ko, and D. E. Kim, Isolated terawatt attosecond hard x-ray pulse generated from single current spike, Sci. Rep. **8**, 1 (2018).
[18] E. Prat and S. Reiche, Simple Method to Generate Terawatt-Attosecond X-Ray Free-Electron-Laser Pulses, Phys. Rev. Lett. **114**, 244801 (2015).

[19] J. Amann, W. Berg, V. Blank, F.-J. Decker, Y. Ding, P. Emma, Y. Feng, J. Frisch, D. Fritz, J. Hastings *et al.*, Demonstration of self-seeding in a hard-x-ray free-electron laser, Nat. Photonics **6**, 693 (2012).

[20] I. Inoue, T. Osaka, T. Hara, T. Tanaka, T. Inagaki, T. Fukui, S. Goto, Y. Inubushi, H. Kimura, R. Kinjo *et al.*, Generation of narrow-band x-ray free-electron laser via reflection self-seeding, Nat. Photonics **13**, 319 (2019).

[21] C.-K. Min, I. Nam, H. Yang, G. Kim, C. H. Shim, J. H. Ko, M.-H. Cho, H. Heo, B. Oh, Y. J. Suh *et al.*, Hard x-ray self-seeding commissioning at pal-xfel, J. Synchrotron Radiat. **26**, 1101 (2019).

[22] A. Halavanau, F. J. Decker, Y. Ding, C. Emma, Z. Huang, J. Krzywinski, A. A. Lutman, G. Marcus, C. Pellegrini, and D. Zhu, Generation of high peak power hard x-rays at LCLS-ii with double bunch self-seeding, https://www.osti.gov/biblio/1560969 (2019).

[23] D. Strickland and G. Mourou, Compression of amplified chirped optical pulses, Opt. Commun. **55**, 447 (1985).

[24] D. Papadopoulos, J. Zou, C. Le Blanc, G. Chériaux, P. Georges, F. Druon, G. Mennerat, P. Ramirez, L. Martin, A. Fréneaux *et al.*, The apollon 10 pw laser: Experimental and theoretical investigation of the temporal characteristics, High Power Laser Sci. Eng. **4** (2016).

[25] D. Gauthier, E. Allaria, M. Coreno, I. Cudin, H. Dacasa, M. B. Danailov, A. Demidovich, S. Di Mitri, B. Diviacco, E. Ferrari *et al.*, Chirped pulse amplification in an extreme-ultraviolet free-electron laser, Nat. Commun. **7**, 13688 (2016).

[26] C. Pellegrini, High power femtosecond pulses from an x-ray SASE-FEL, Nucl. Instrum. Methods Phys. Res., Sect. A **445**, 124 (2000).

[27] S. Krinsky and Z. Huang, Frequency chirped self-amplified spontaneous-emission free-electron lasers, Phys. Rev. ST Accel. Beams **6**, 050702 (2003).

[28] F.-J. Decker, K. L. Bane, W. Colocho, S. Gilevich, A. Marinelli, J. C. Sheppard, J. L. Turner, J. J. Turner, S. L. Vetter, A. Halavanau, and C. Pellegrini, Tunable x-ray free electron laser multi-pulses with nanosecond separation, Sci. Rep. **12**, 1 (2022).

[29] S. Reiche, Genesis 1.3: A fully 3D time-dependent FEL simulation code, Nucl. Instrum. Methods Phys. Res., Sect. A **429**, 243 (1999).

[30] H. Li, Source code of xcpa, https://github.com/haoyuanli93/XCPA (2022).

[31] B. W. Batterman and H. Cole, Dynamical diffraction of x rays by perfect crystals, Rev. Mod. Phys. **36**, 681 (1964).

[32] O. Martinez, J. Gordon, and R. Fork, Negative group-velocity dispersion using refraction, JOSA A **1**, 1003 (1984).

[33] F. Decker, S. Gilevich, Z. Huang, H. Loos, A. Marinelli, C. Stan, J. Turner, Z. Van Hoover, S. Vetter *et al.*, Two bunches with ns-separation with lcls, in *Proceedings of the 37th International Free Electron Laser Conference (FEL 2015)*, edited by H. S. Kang, D.-E. Kim, and V. R. W. Schaa (JACoW, Geneva, Switzerland, 2015), p. WEP023.

[34] O. Martinez, 3000 times grating compressor with positive group velocity dispersion: Application to fiber compensation in $1.3 - 1.6$ μm region, IEEE J. Quantum Electron. **23**, 59 (1987).

[35] See Supplemental Material at http://link.aps.org/supplemental/10.1103/PhysRevLett.129.213901 for detailed derivation of the energy dependence of the light path length of the stretcher and the compressor is summarized in the supplemental material.

[36] C. P. Schwartz *et al.*, Angstrom-Resolved Interfacial Structure in Buried Organic-Inorganic Junctions, Phys. Rev. Lett. **127**, 096801 (2021).

[37] E. Berger, S. Jamnuch, C. B. Uzundal, C. Woodahl, H. Padmanabhan, A. Amado, P. Manset, Y. Hirata, Y. Kubota, S. Owada *et al.*, Extreme ultraviolet second harmonic generation spectroscopy in a polar metal, Nano Lett. **21**, 6095 (2021).

[38] C. B. Uzundal, S. Jamnuch, E. Berger, C. Woodahl, P. Manset, Y. Hirata, T. Sumi, A. Amado, H. Akai, Y. Kubota, S. Owada, K. Tono, M. Yabashi, J. W. Freeland, C. P. Schwartz, W. S. Drisdell, I. Matsuda, T. A. Pascal, A. Zong, and M. Zuerch, Polarization-Resolved Extreme-Ultraviolet Second-Harmonic Generation from $LiNbO_3$, Phys. Rev. Lett. **127**, 237402 (2021).

[39] S. Tanaka, Ultrafast relaxation dynamics of the one-dimensional molecular chain: The time-resolved spontaneous emission and exciton coherence, J. Chem. Phys. **119**, 4891 (2003).

[40] S. Tanaka and S. Mukamel, Simulation of optical and x-ray sum frequency generation spectroscopy of one-dimensional molecular chain, J. Electron Spectrosc. Relat. Phenom. **136**, 185 (2004).

[41] R. Pandey and S. Mukamel, Simulation of x-ray absorption near-edge spectra and x-ray fluorescence spectra of optically excited molecules, J. Chem. Phys. **124**, 094106 (2006).

[42] L. Campbell and S. Mukamel, Simulation of x-ray absorption near edge spectra of electronically excited ruthenium tris-2, 2′-bipyridine, J. Chem. Phys. **121**, 12323 (2004).

[43] O. Berman and S. Mukamel, Current profiles of molecular nanowires: Density-functional theory green's function representation, Phys. Rev. B **69**, 155430 (2004).